ACS APPLIED MATERIALS & INTERFACES

www.acsami.org

Research Article

Unraveling the Impact of Graphene Addition to Thermoelectric $SrTiO_3$ and La-Doped $SrTiO_3$ Materials: A Density Functional Theory Study

Joshua Tse,[⊥] Alex Aziz,[⊥] Joseph M. Flitcroft,[⊥] Jonathan M. Skelton,* Lisa J. Gillie, Stephen C. Parker, David J. Cooke, and Marco Molinari*

Cite This: *ACS Appl. Mater. Interfaces* 2021, 13, 41303−41314

Read Online

ACCESS | Metrics & More | Article Recommendations | Supporting Information

ABSTRACT: We present a detailed theoretical investigation of the interaction of graphene with the SrO-terminated (001) surface of pristine and La-doped $SrTiO_3$. The adsorption of graphene is thermodynamically favorable with interfacial adsorption energies of −0.08 and −0.32 J/m^2 to pristine $SrTiO_3$ and La-doped $SrTiO_3$ surfaces, respectively. We find that graphene introduces C 2p states at the Fermi level, rendering the composite semimetallic, and thus the electrical properties are predicted to be highly sensitive to the amount and quality of the graphene. An investigation of the lattice dynamics predicts that graphene adsorption may lead to a 60−90% reduction in the thermal conductivity due to a reduction in the phonon group velocities, accounting for the reduced thermal conductivity of the composite materials observed experimentally. This effect is enhanced by La doping. We also find evidence that both La dopant ions and adsorbed graphene introduce low-frequency modes that may scatter heat-carrying acoustic phonons, and that, if present, these effects likely arise from stronger phonon−phonon interactions.

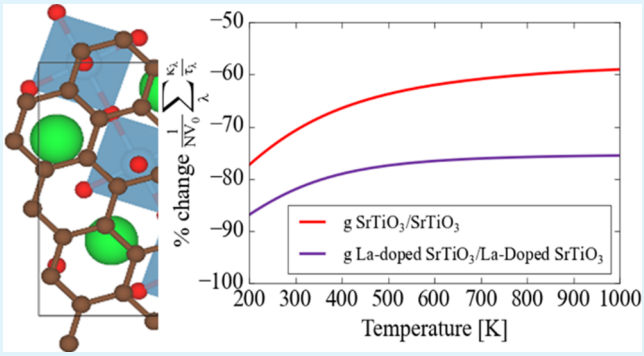

KEYWORDS: *thermoelectrics, graphene/strontium titanate composite materials, electronic structure, structural dynamics, thermal transport, graphene adsorption on perovskite oxides*

INTRODUCTION

With continued growth in global energy consumption, greater importance must be placed on moving away from fossil fuels to clean energy solutions. An increase in renewable energy generation must also be delivered alongside technologies to improve the efficiency of existing energy-intensive systems such as internal combustion engines to mitigate the worst effects of climate change.[1] Thermoelectric (TE) power generation is a promising method to reduce energy consumption and increase efficiencies by recycling waste heat back to electrical energy.[2] TE devices have already found applications in the aerospace, automotive and heavy manufacturing industries, and in remote power generation, and further improvements to their performance would allow them to compete economically with traditional sources of primary energy generation.[3−5]

The performance of a TE material is determined by the dimensionless figure of merit $ZT = S^2\sigma T/\kappa$, where S is the Seebeck coefficient, σ is the electrical conductivity, $\kappa = \kappa_{el} + \kappa_{latt}$ is the thermal conductivity, and T is the temperature. The thermal conductivity has contributions from the electrical thermal conductivity κ_{el} and the lattice (phonon) thermal conductivity κ_{latt}. Methods for optimizing ZT include doping and dimensionality reduction[6−9] through nanostructuring[10−12] and nanocompositing.[8,13,14] However, improving TE performance is a complex process due to the interdependence of the electrical properties—increasing σ by increasing the carrier concentration n improves the power factor $S^2\sigma$ but also increases κ_{el} and tends to decrease S.

Most TE materials currently on the market are alloys containing bismuth, antimony, and tellurium,[15−18] which are rare, toxic, and/or expensive. While the highest ZT are currently obtained with chalcogenide TEs,[19,20] recent work has shown that metal oxides[20−22] such as $CaMnO_3$,[23] $SrTiO_3$,[24−27] M_2CoO_3,[28] $BaTiO_3$,[29] tungsten bronze,[30,31] $Bi_2Sr_2Co_{1.8}O_y$,[32] In_2O_3,[33] and $La_{1/3}NbO_3$[34] may be promising alternatives to conventional TE materials while being made from cheaper,

Received: June 10, 2021
Accepted: August 6, 2021
Published: August 18, 2021

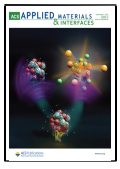

more earth-abundant, and less toxic materials.[35,36] Among the potential oxide TEs, strontium titanate ($SrTiO_3$; STO) shows promise due to its thermal stability at high temperature and tolerance to doping.[26,27,37] Bulk $SrTiO_3$ has a relatively poor *ZT*, and thus doping has been extensively explored as a possible route to improving its performance with examples including substituting Sr sites with rare-earth elements such as La[38,39] and Ti sites with other transition metals such s Nb.[40−42] La doping has been shown to promote the formation of A-site vacancies, which both increases the electrical conductivity and decreases the thermal conductivity through enhanced phonon scattering.[43] Doping with La under reducing conditions further leads to the formation of oxygen vacancies, which decreases the thermal conductivity while having minimal impact on the electrical conductivity. Wang *et al.*[38] showed that doping $SrTiO_3$ with 12% Dy and 8% La increased the *ZT* from 0.05 to 0.36 at ∼800 °C.

As an alternative to doping, strain engineering,[44,45] grain boundary engineering,[10,11,46,47] and nanocompositing $SrTiO_3$ with materials such as graphene also have the potential to improve the TE performance. In the latter case, whereas a graphene-based TE would perform poorly due to its large thermal conductivity, the addition of graphene to conventional-[48,49] and oxide-based[8,13,14,50,51] TEs has been shown to produce synergistic improvements in the *ZT*. Lin *et al.*[13] investigated the addition of graphene to lanthanum-doped (LSTO) and noted a widening of the operating window to room temperature, a decrease in the thermal conductivity, and a significant increase in the electrical conductivity. The best results were obtained when 0.6 wt % of graphene was added, achieving a *ZT* of 0.42 at room temperature and 0.36 at 750 °C, amounting to a 280% improvement over pure LSTO. Bantawal *et al.*[50] and Baran *et al.*[52] investigated the electronic structure of graphene−$SrTiO_3$ composites and found that carbon states were present at the Fermi level within the $SrTiO_3$ band gap. The latter study[52] also showed that by altering the $SrTiO_3$ surface termination the electrical properties of the material could be tuned to optimize the electrical conductivity and to obtain both p and n-type transport.

In this work, we extend these previous studies by performing further detailed characterization of STO/LSTO−graphene composites, including modeling the structural dynamics and elucidating the impact of graphene adsorption on the thermal transport. We find that the nanocompositing produces surface interactions that impact both the electronic and thermal properties of the composite. Analysis of the electronic density of states displays characteristic fingerprints of graphene, which are reflected in the electrical properties of the composite, and analysis of the phonon spectra and group velocities indicates that the La doping and graphene adsorption are both likely to suppress the heat transport in the composite materials. These results provide further fundamental insight into how surfaces and interfaces can be exploited through nanocompositing, providing a firm foundation for the discovery and optimization of future high-performance TEs.

METHODOLOGY

Calculations were performed using pseudopotential plane-wave density functional theory (DFT) as implemented in the Vienna *Ab initio* Simulation Package (VASP) code.[53−56] We employed the Perdew−Burke−Ernzerhof (PBE) generalized-gradient approximation (GGA) functional[57,58] with the DFT-D3 dispersion correction[59] to account for van der Waals interactions. The projector augmented-wave (PAW) method was used to describe interactions between the core and valence electrons, with the following valence configurations: O—$2s^22p^4$; C—$2s^22p^2$; Sr—$4s^24p^65s^2$, Ti—$3d^24s^2$, and La—$5s^25p^66s^25d^1$.[60,61] A kinetic energy cutoff of 520 eV was used to represent the Kohn−Sham orbitals, which was determined from explicit convergence testing. Γ-centered ***k***-point grids with 6 × 6 × 6 and 4 × 4 × 1 subdivisions were used to integrate the Brillouin zones of bulk $SrTiO_3$ and surface models, respectively. Surface models were generated with an initial vacuum spacing of 20 Å between periodic images, and a dipole correction was applied in the direction of the surface normal. The electronic energies were converged to 10^{-6} eV, and geometry optimizations were performed until the magnitude of the forces on the atoms were below 10^{-2} eV/Å. For the surface models, geometry optimizations were performed with the cell shapes and volumes fixed.

Transport coefficients were evaluated by solving the linearized Boltzmann transport equations within the constant relaxation-time approximation using the BoltzTraP code.[62] The band energies of bulk $SrTiO_3$ and the surface models were calculated non-self-consistently on dense 50 × 50 × 50 and 20 × 20 × 1 ***k***-point meshes, respectively, and Fourier interpolation was used to increase these densities by a further 5×. The BoltzTraP results were compared to calculations using the BoltzWann code,[63,64] details of which are given in the SI. To obtain the charge carrier concentration, we used Boltzmann transport analysis, where the chemical potential is directly related to the carrier concentration. As the chemical potential is shifted into the valence or conduction bands, the number of hole or electron carriers increases. By interpolating the density of states (DOS), the number of carriers at any given chemical potential can thus be determined. To validate the BoltzTrap and BoltzWann methods, we calculated the Seebeck coefficient of bulk $SrTiO_3$ as a function of carrier concentration (Figure S5) and as a function of temperature at a fixed carrier concentration corresponding to the bottom of the conduction band (Figure S6).[62,65] The calculations with the two methods give similar results (Figures S7 and S8). We also compared the band structures of bulk $SrTiO_3$ and the surface models obtained from our DFT calculations and by Wannier interpolation using the Wannier functions employed in our transport calculations (Figures S2−S4).

Finally, we employed the Phonopy[66] and Phono3py codes[68] to compute for the slab models the harmonic force constants, phonon spectra, phonon group velocities, and quantities related to the lattice thermal conductivity. In these calculations, VASP was used as the force calculator to obtain the harmonic force constants using the supercell finite-displacement method.[67] Atomic displacements were generated in 2 × 2 × 1 supercells, and accurate single-point force calculations were performed with a 500 eV cutoff energy and proportionally reduced 2 × 2 × 1 ***k***-point meshes. For these calculations, the PAW projection was performed in reciprocal space, and an auxiliary charge−density grid with 8× the density of points was used when evaluating the forces.

RESULTS AND DISCUSSION

Structure and Energetics. The optimized surface models investigated in this work are shown in Figure 1. Low-energy ion-scattering (LEIS) experiments have shown that perovskite surfaces display a dominant AO termination at elevated temperature,[69−72] based on which we chose the SrO-

https://doi.org/10.1021/acsami.1c10865
ACS Appl. Mater. Interfaces 2021, 13, 41303−41314

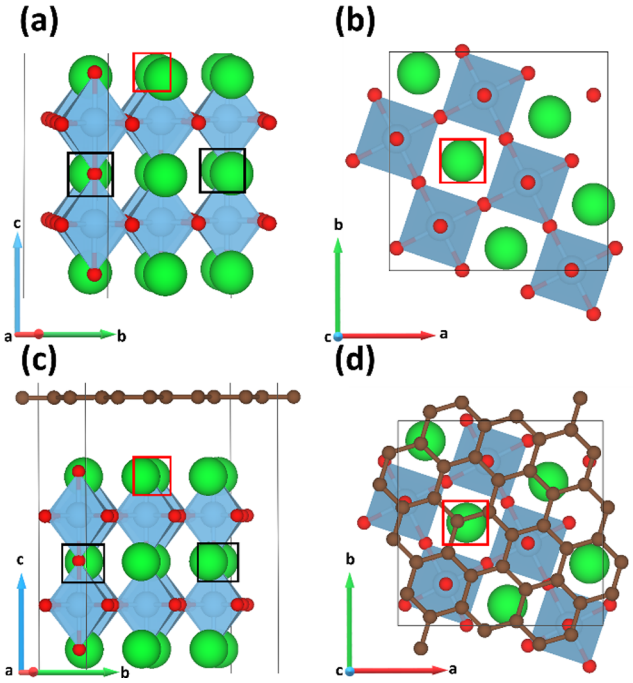

Figure 1. Surface structures investigated in this work. (a, b) $SrTiO_3$ surface—(a) side and (b) top view. (c, d) graphene-decorated $SrTiO_3$ surface—(c) side and (d) top view. The black and red squares mark the positions of La dopant atoms and charge-balancing Sr vacancies in the corresponding La-doped $SrTiO_3$ surface models.

terminated {001} surface of $SrTiO_3$ as our starting point. An appropriate slab model was constructed from bulk cubic $SrTiO_3$, consisting of 20 $SrTiO_3$ and 5 SrO formula units (Figure 1). The additional 5 SrO units are required to form a complete monolayer, and the top and bottom surfaces of the slab models are therefore identical. A single-layer graphene model comprising 30 C atoms was then constructed and combined with the $SrTiO_3$ surface, with the lattice vectors of both components redefined using the METADISE code[73] to reduce the residual strain on the graphene sheet to ~0.90%.[52]

Models of La-doped $SrTiO_3$ with and without adsorbed graphene were further generated by introducing two Sr vacancies on each side of the corresponding $SrTiO_3$ slabs and substituting four subsurface Sr atoms with La to maintain overall charge neutrality, which we found to be the most stable arrangement.[52]

The surface energies of the $SrTiO_3$ and La-doped $SrTiO_3$ slab models were calculated according to

$$20(SrTiO_3)_{bulk} + 5(SrO)_{bulk} \rightarrow (Sr_{25}Ti_{20}O_{65})_{surf} \quad (1)$$

$$\gamma_S = (E_S - 20E_{B,SrTiO_3} - 5E_{B,SrO})/2A \quad (2)$$

$$19(SrTiO_3)_{bulk} + (TiO_2)_{bulk} + 2(La_2O_3)_{bulk} \rightarrow (Sr_{19}La_4Ti_{20}O_{65})_{surf} \quad (3)$$

$$\gamma_S = (E_S - 19E_{B,SrTiO_3} - 1E_{B,TiO_2} - 2E_{B,La_2O_3})/2A \quad (4)$$

where the E_S and E_B are the energies of the surface and bulk models, respectively, and A is the surface area. We calculate a γ_S of 1.76 J/m^2 for $SrTiO_3$ and 1.86 J/m^2 for La-doped $SrTiO_3$.

The graphene layer adsorbs to the $SrTiO_3$ surfaces at a distance of 3.23 Å, in good agreement with the 3.19 Å distance obtained in the calculations by Zou *et al.*[74] The graphene adsorption and interfacial adsorption energies were calculated as

$$(Sr_{25}Ti_{20}O_{65})_{surf} + 30(C)_{graph} \rightarrow [(Sr_{25}Ti_{20}O_{65})(C)_{30}]_{g-surf} \quad (5)$$

$$(Sr_{19}La_4Ti_{20}O_{65})_{surf} + 30(C)_{graph} \rightarrow [(Sr_{19}La_4Ti_{20}O_{65})(C)_{30}]_{g-surf} \quad (6)$$

$$E_{Ads,graph} = (E_{g-surf} - E_{surf} - E_{graph})/n_C \quad (7)$$

$$\gamma_{Ads} = (E_{g-surf} - E_{surf} - E_{graph})/A \quad (8)$$

where $E_{g\text{-}surf}$ and E_{surf} are the energies of the graphene-coated and pristine surfaces, respectively, and E_{graph} is the energy of the graphene sheet with n_C = 30 carbon atoms. We note that our models of pristine graphene and the graphene-decorated surfaces have the same number of C atoms. We obtain $E_{Ads,\ graph}$ = −0.01 and −0.05 eV per C atom for the $SrTiO_3$ and La-doped $SrTiO_3$ surfaces, respectively, which give the magnitude of the attachment energy for graphene to the oxide surfaces and indicate a small but energetically favorable adsorption. The interfacial adsorption energies were calculated to be −0.08 and −0.32 J/m^2, respectively, for graphene adsorbed to pristine $SrTiO_3$ and La-doped $SrTiO_3$ surfaces. Such small energies are similar to the average binding energy of graphene onto the $SrTiO_3$ (100) surfaces of 0.056 eV per C atom calculated by Zou *et al.*[74] The difference in energy may be due to the lower level of strain in the graphene sheets in this work (0.9 vs 2.5% in the study in ref 74).

Finally, the energies for La doping were calculated as

$$(Sr_{25}Ti_{20}O_{65})_{surf} + 2(La_2O_3)_{bulk} \rightarrow (Sr_{19}La_4Ti_{20}O_{65})_{surf} + 6(SrO)_{bulk} \quad (9)$$

$$[(Sr_{25}Ti_{20}O_{65})(C)_{30}]_{g-surf} + 2(La_2O_3)_{bulk} \rightarrow [(Sr_{19}La_4Ti_{20}O_{65})(C)_{30}]_{g-surf} + 6(SrO)_{bulk} \quad (10)$$

$$E_{D,La} = (E_{La,surf} + 6E_{B,SrO} - E_{surf} - 2E_{B,La_2O_3})/n_{La} \quad (11)$$

where the E_B are the bulk energies of SrO and La_2O_3, $E_{La,surf}$ and E_{surf} are the energies of the La-doped and pristine surfaces, respectively, and n_{La} is the number of La dopant atoms. We calculate an $E_{D,La}$ of 0.57 eV per La atom for the $SrTiO_3$ surfaces and 0.28 eV per La for the graphene-coated $SrTiO_3$ (g-$SrTiO_3$) surfaces, indicating that the energetic penalty for La doping is substantially reduced in the presence of graphene.

Electronic Structure. We calculate direct and indirect band gaps of 2.0 and 1.65 eV for bulk $SrTiO_3$ (Figure S2). The former may be compared to values of 2.74 eV using the LDA[75] and 2.34 eV using the PBE GGA.[76] Similarly, our calculated indirect gap can be compared to values of 2.14[75,77] and 1.85 eV using the LDA[78] and 1.99 eV using PBE.[76] Our calculations deviate from the experimental values of 3.75 and 3.25 eV (direct/indirect) due to the well-known band gap underestimation inherent in (semi-)local DFT.[79] The underestimation of our calculated band gaps compared to other computational literature is likely due to the inclusion of a van der Waals correction (DFT-D3); indeed, Holmström *et al.*[80,81] calculated a band gap of 1.76−2.00 eV with PBE-D3, which is in keeping with our results. Despite the band gap under-

https://doi.org/10.1021/acsami.1c10865
ACS Appl. Mater. Interfaces 2021, 13, 41303−41314

estimation, our calculations still correctly predict $SrTiO_3$ to be a semiconductor and thus do not affect the qualitative analysis of the electronic structure, and, most importantly, the quantitative comparison between the slab models.

The electronic density of states (DOS) of $SrTiO_3$ and La-doped $SrTiO_3$ surface models indicate them to be semiconductors. As for bulk $SrTiO_3$, the surfaces are predicted to have an indirect band gap (Figures S3 and S4). The orbital-projected partial density of states (Figure 2a,c) shows an asymmetric DOS with sharp peaks in the valence band. At the PBE-D3 level of theory, the calculated band gaps for $SrTiO_3$ and La-doped $SrTiO_3$ are 1.75 and 1.89 eV, respectively. These are in line with previous calculations on the SrO-terminated (001) surface, which estimated band gaps of 1.72−2.01 eV[80] (PBE-D3) and 1.86 eV (LDA).[78] In agreement with both theory and experiment, we find that the valence band maximum and conduction band minimum are dominated by O 2p and Ti 3d states, respectively.[79] The addition of graphene to the surface introduces C 2p states into the $SrTiO_3$ band gap (Figure 2b,d). However, the contribution of these states at the Fermi level is relatively small, and as such that the composite could be classified as a semimetal, that is, graphene does not induce metallic behavior in bulk $SrTiO_3$, but rather introduces gap states that allow for metallic conduction with a small number of carriers. Previous studies using the (bare) PBE functional predicted a similar introduction of C 2p states at the Fermi level when $SrTiO_3$ is composited with porous graphene (i.e., with carbon vacancies), irrespective of the concentration of pores.[50]

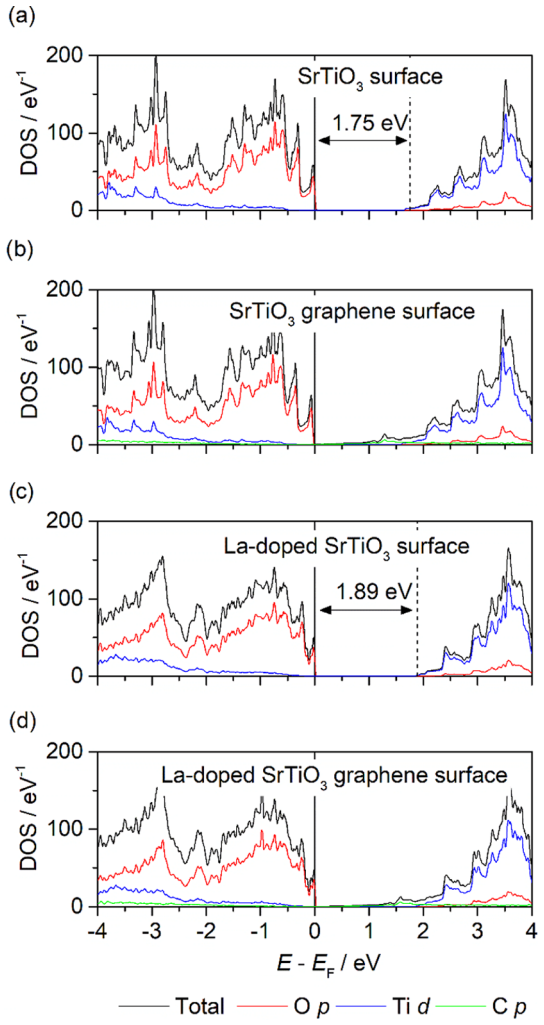

Figure 2. Total and orbital-projected electronic densities of states (DOS) from DFT calculations showing the composition of the valence and conduction bands in $SrTiO_3$ and La-doped $SrTiO_3$ surfaces with and without adsorbed graphene sheets.

Electronic Transport. It is clear from Figure 2 that the interaction of graphene with $SrTiO_3$ surfaces intrinsically alters the electronic structure and as such is expected to impact upon the electronic transport and thermoelectric properties. The three crucial properties controlled by the electronic structure are the Seebeck coefficient S, the electrical conductivity σ, and the electronic part of the thermal conductivity κ_{el}.

Figure 3 shows calculations of these three properties as a function of carrier concentration for the pristine and graphene-adsorbed surfaces. The same properties as a function of chemical potential are presented in Figure S10. Figure 3a compares the Seebeck coefficients of the pristine $SrTiO_3$ and La-doped $SrTiO_3$ surfaces as a function of carrier concentration. Within the constant relaxation-time approximation (CRTA) used by BoltzTraP, σ and κ_{el} are determined with respect to an unknown electron relaxation time τ, while S is independent of this parameter. Within this model, we obtain Seebeck coefficients of 1 333 and 1 475 μV/K at 600 K for the $SrTiO_3$ and La-doped $SrTiO_3$ surfaces, respectively (Figure 3a). Comparable values of 1342 and 1498 μV/K are obtained using BoltzWann (Figure S7). A general feature of the DOS of both models is an asymmetry arising from sharper features at valence band edges than at conduction band edges. For an intrinsic (undoped) semiconductor, where no charge carriers are present (p−n = 0), the Seebeck coefficient is governed solely by the gradient of the DOS at the band edges. In undoped $SrTiO_3$, the larger gradient of the DOS at the valence band edge compared to the conduction band edge leads to a larger p-type contribution and a positive S (Figure S9). At higher temperatures, the smoothing out of the Fermi−Dirac distribution reduces the asymmetry in the DOS and S becomes negative, indicating n-type conductivity.[82] The larger Seebeck coefficient of the La-doped $SrTiO_3$ surface compared to the $SrTiO_3$ surface is consistent with the steeper states in the DOS of the former (Figure 2).

These values represent the maximum theoretical value that could be obtained for ideal, defect-free compositions. In reality, all materials contain defects that promote n or p-type conductivity, and the carrier concentrations are therefore heavily dependent on the material preparation. Both bulk and thin-film $SrTiO_3$ show n-type conductivity,[83,84] so we calculated the carrier concentrations relative to the bottom of the conduction band. This method is valid within the rigid-band approximation[65] and has been used on similar perovskite systems. We obtain a carrier concentration of $\sim 10^{20}$ cm^{-3} for bulk $SrTiO_3$ (Figure S6) and about 2.6×10^{20} cm^{-3} for the $SrTiO_3$ surface model, which is in line with the $\sim 3.5 \times 10^{20}$ cm^{-3} reported by Ravichandran *et al.* for undoped $SrTiO_3$ thin films.[84] Based on recent experiments,[13] we also report values of S at carrier concentrations of 3×10^{19} cm^{-3}. Figure 4a shows the Seebeck coefficients obtained for the surface models using BoltzTraP, and comparisons with BoltzWann are given in Figures S5−S7. The absolute value of the Seebeck coefficient increases with temperature, as is observed in bulk $SrTiO_3$ at a fixed carrier concentration, and has previously been reported for bulk[85] and thin-film samples.[84]

https://doi.org/10.1021/acsami.1c10865
ACS Appl. Mater. Interfaces 2021, 13, 41303−41314

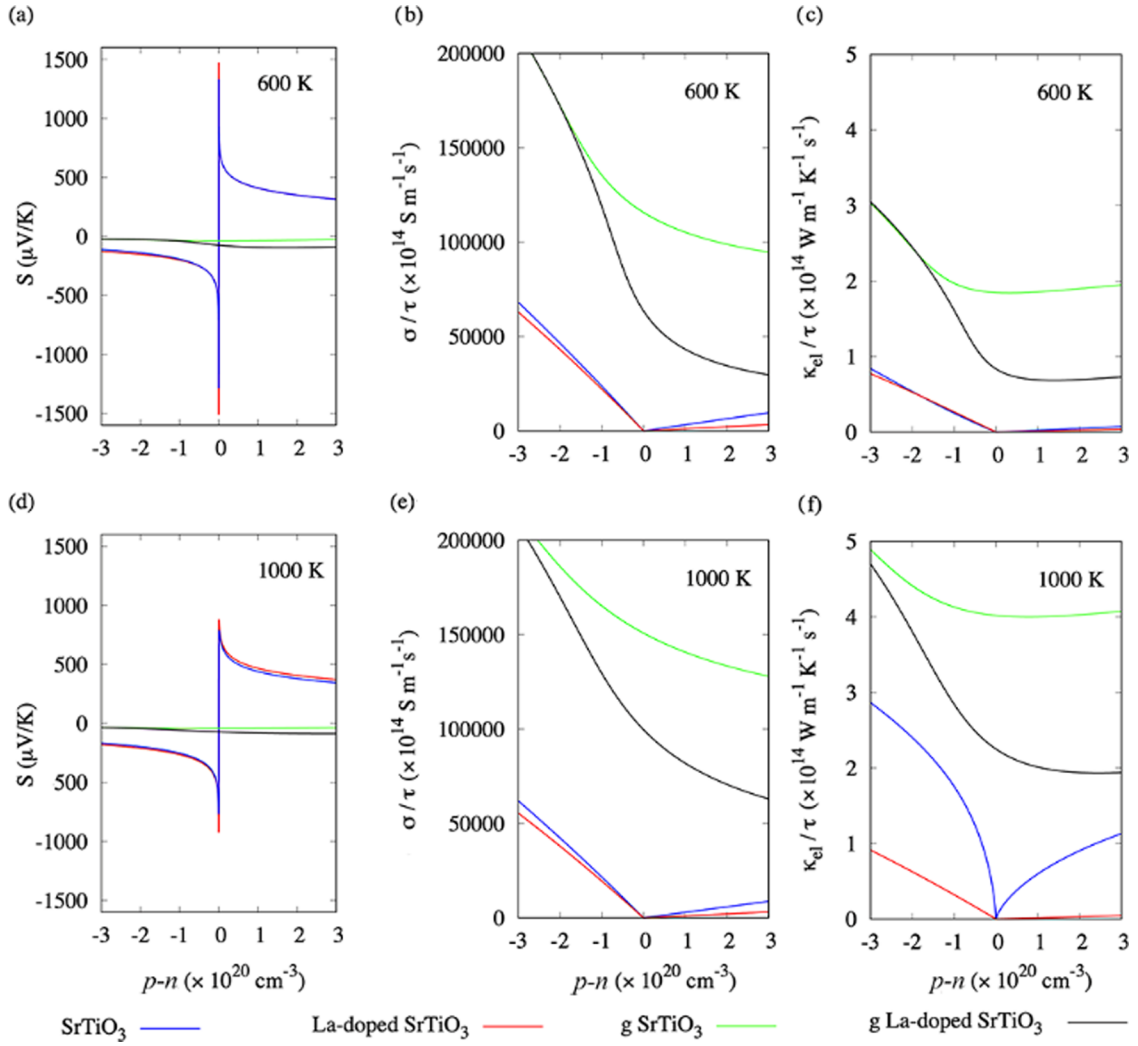

Figure 3. Seebeck coefficient S (a, d), electrical conductivity σ/τ (b, e), and electronic thermal conductivity κ_{el}/τ (c, f) as a function of carrier concentration p−n for pristine and graphene-adsorbed $SrTiO_3$ and La-doped $SrTiO_3$ surfaces at T = 600 (a−c) and 1000 K (d−f), calculated using the BoltzTraP code.

The electronic structures in Figure 2 show that the addition of graphene introduces C 2p states into the $SrTiO_3$ band gap, resulting in a semimetallic electronic structure for both graphene-adsorbed surfaces. As shown in Figures S10a, 3a, and 4a, this results in an extremely low Seebeck coefficient at 600 K, with an order of magnitude difference in the maximum absolute values between the pristine and graphene-adsorbed surfaces. While inconsistent with the findings of Lin *et al.*,[13] this is most likely due to the effective concentration of graphene in our models—whereas we have an effectively infinite graphene layer adsorbed onto the surfaces of the perovskite material, which would correspond to an ∼8 wt % composite, the highest concentration used in the experimental work is a much smaller 1 wt %. However, we can infer from the discrepancy that the electrical performance of these composite TEs is likely to be highly sensitive to the amount of graphene present and also its quality in terms of flake size and defect concentration, as these would strongly influence both the electrical properties of the graphene sheets and their interaction with the perovskite surfaces. Introducing high concentrations of graphene in graphene-oxide composites would lead to the thermoelectric properties being driven mostly by the graphene component, and from this perspective, our results are qualitatively in line with the Seebeck coefficients predicted for graphene from tight-binding models.[86]

At higher carrier concentrations, S decreases with temperature (Figure 4a,d), implying that the oxide component retains some influence on the properties of the composite. This is opposite to what is seen for carbon nanoribbons interacting with $SrTiO_3$ surfaces, where S instead increases with temperature in the composite material.[52]

As noted above, solving the Boltzmann transport equations within the constant relaxation-time approximation yields the electrical conductivity σ and electronic thermal conductivity κ_{el} with respect to an unknown electron scattering time τ. τ incorporates complex physical phenomena including electron−phonon coupling and cannot, at present, practically be calculated from the first principles. For completeness, we plot these two properties as a function of carrier concentration (Figure 3), chemical potential (Figure S10), and temperature (Figure 4) and again observe substantially different behavior for the pristine and graphene-adsorbed systems. As noted above, the graphene-adsorbed systems have semimetallic character, since electronic states cross the Fermi level in graphene-adsorbed models, and we predict p-type conduction. The change from semiconducting to metallic behavior has a

https://doi.org/10.1021/acsami.1c10865
ACS Appl. Mater. Interfaces 2021, 13, 41303−41314

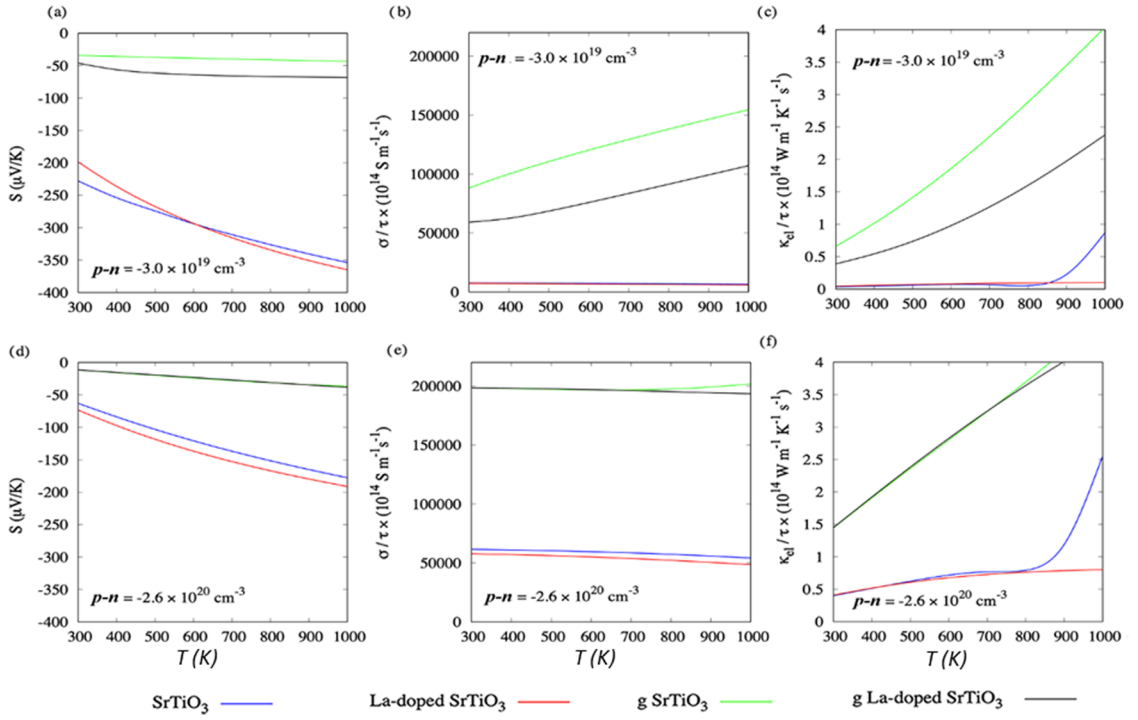

Figure 4. Seebeck coefficient S (a,d), electrical conductivity σ/τ (b,e), and electronic thermal conductivity κ_{el}/τ (c,f) as a function of temperature for pristine and graphene-adsorbed $SrTiO_3$ and La-doped $SrTiO_3$ surfaces, with carrier concentrations of p−n = -3.0×10^{19} cm^{-3} (a−c) and -2.6×10^{20} cm^{-3} (d−f), calculated using the BoltzTraP code.

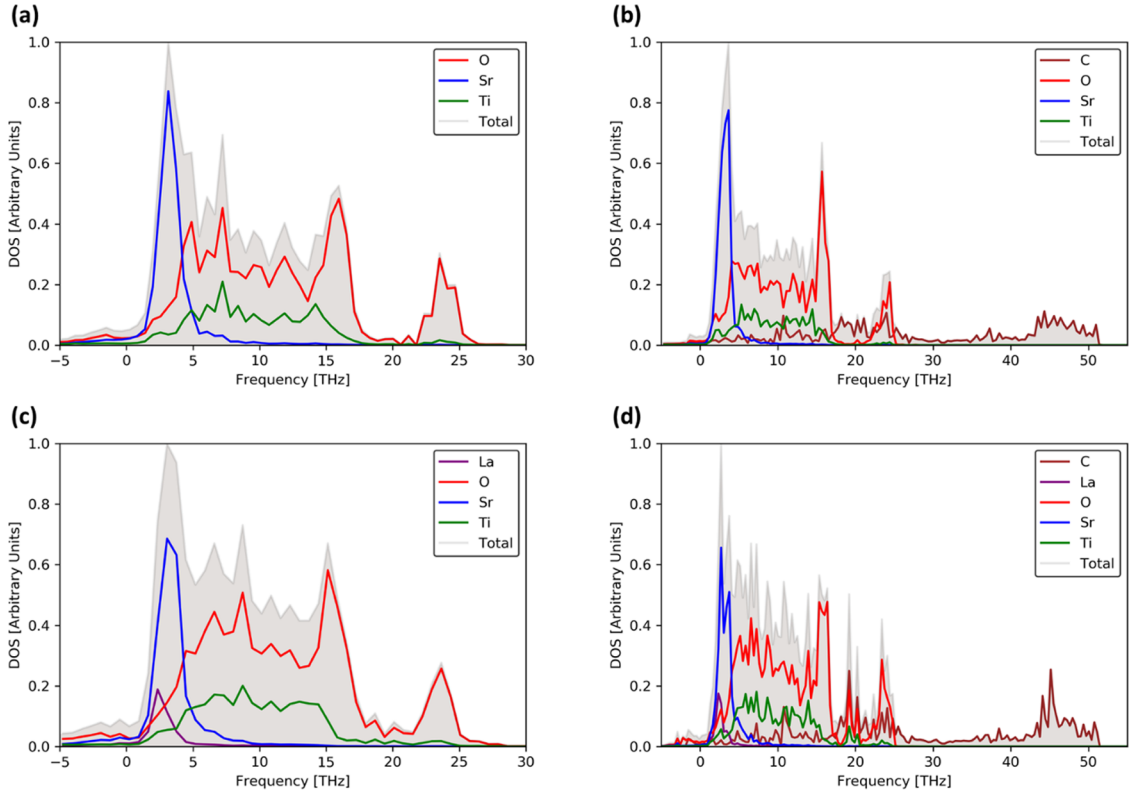

Figure 5. Atom-projected partial phonon density of states (PDOS) of the $SrTiO_3$ surface model (a), the $SrTiO_3$ surface with adsorbed graphene (b), the La-doped $SrTiO_3$ surface model (c), and the La-doped $SrTiO_3$ surface with adsorbed graphene (d).

large effect on the transport properties, resulting in an increased σ and κ_{el} together with a reduced S, since the latter is inversely related to the number of free carriers.[87]

Lattice Dynamics and Thermal Transport. The lattice component of the thermal conductivity κ_{latt} can be calculated using the second-order (harmonic) and third-order (anhar-

https://doi.org/10.1021/acsami.1c10865
ACS Appl. Mater. Interfaces 2021, 13, 41303−41314

monic) force constants. However, obtaining the latter is computationally very expensive and is prohibitive for large systems such as our surface models. For this reason, we chose instead to examine the atom-projected phonon density of states (PDOS), the weighted two-phonon joint density of states (wJDOS), and the mode group velocities, all of which can be computed using the second-order force constants, to assess how changes in the phonon spectrum due to the doping and graphene adsorption are likely to impact the heat transport.[13]

Figure 5 compares the atom-projected phonon DOS (PDOS) curves of the four surface models. The PDOS curves of La-doped surfaces show large contributions from La at low frequencies, suggesting that localized "rattling" modes involving La^{3+} cations could in principle couple strongly to low-frequency acoustic modes to suppress transport through the TiO_6 octahedral framework. There is also a significant contribution from C to the low-frequency DOS in the graphene models, which likewise suggests that the graphene and $SrTiO_3$ modes may also couple to suppress the thermal transport of both components.

Within the single-mode relaxation-time approximation (RTA) to the phonon Boltzmann transport equation, the lattice thermal conductivity tensors $\boldsymbol{\kappa}_{\text{latt}}(T)$ can be written as a sum of contributions $\boldsymbol{\kappa}_\lambda(T)$ from the individual phonon modes λ as

$$\boldsymbol{\kappa}_{\text{latt}}(T) = \frac{1}{NV_0}\sum_\lambda \boldsymbol{\kappa}_\lambda(T) = \frac{1}{NV_0}\sum_\lambda C_\lambda(T)\boldsymbol{\nu}_\lambda \otimes \boldsymbol{\nu}_\lambda \tau_\lambda(T) \tag{12}$$

where C_λ are the modal heat capacities, $\boldsymbol{\nu}_\lambda$ are the group velocities, V_0 is the volume of the unit cell, N is the number of reciprocal-space wavevectors ($\mathbf{q}$) included in the sum over the Brillouin zone, and τ_λ are the phonon lifetimes given by

$$\tau_\lambda(T) = \frac{1}{2\Gamma_\lambda(T)} \tag{13}$$

where Γ_λ are the phonon linewidths obtained as the self-energy from third-order perturbation theory. C_λ and $\boldsymbol{\nu}_\lambda$ are calculated within the harmonic approximation as

$$C_\lambda = k_B\left(\frac{\hbar\omega_\lambda}{k_B T}\right)^2 \frac{\exp[-\hbar\omega_\lambda/k_B T]}{(\exp[-\hbar\omega_\lambda/k_B T]-1)^2} \tag{14}$$

$$\mathbf{v}_\lambda = \frac{\delta\omega_\lambda}{\delta\mathbf{q}_\lambda} = \frac{1}{2\omega_\lambda}\left\langle \mathbf{W}_\lambda \left| \frac{\delta\mathbf{D}(\mathbf{q}_\lambda)}{\delta\mathbf{q}_\lambda} \right| \mathbf{W}_\lambda \right\rangle \tag{15}$$

where ω_λ are the phonon frequencies, $\mathbf{W}_\lambda$ are the corresponding mode eigenvectors, and $\mathbf{D}(\mathbf{q})$ is the dynamical matrix for the wavevector $\mathbf{q}$.

Although the calculation of $\tau_\lambda(T)$ in eq 13 is computationally prohibitive, we can follow the approach of Tang and Skelton[88] and compute the sum over harmonic terms to obtain $\boldsymbol{\kappa}_{\text{latt}}$ with respect to an unknown relaxation time τ^{CRTA} as

$$\frac{\boldsymbol{\kappa}_{\text{latt}}}{\tau^{\text{CRTA}}} \approx \frac{1}{NV_0}\sum_\lambda \frac{\boldsymbol{\kappa}_\lambda}{\tau_\lambda} = \frac{1}{NV_0}\sum_\lambda C_\lambda \boldsymbol{\nu}_\lambda \otimes \boldsymbol{\nu}_\lambda \tag{16}$$

where the modal terms are the same as defined in eq 12. In the following, we consider the diagonal components of $\kappa_{\text{latt}}/\tau^{\text{CRTA}}$ for in-plane transport $1/2\,(xx + yy)$, after rotating the tensors to align with the equivalent directions in bulk STO (see Supporting Information). This analysis shows that one would expect a reduction in $\boldsymbol{\kappa}_{\text{latt}}$ on the order of 60−90% by adsorbing graphene at the surface, based on the changes in the model heat capacities and group velocities (Figure 6). We note

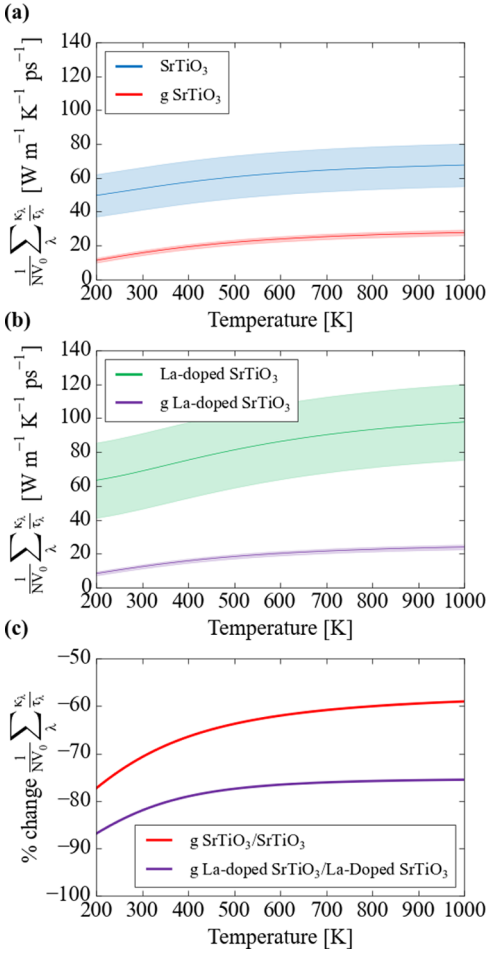

Figure 6. Calculated $\boldsymbol{\kappa}_{\text{latt}}/\tau^{\text{CRTA}}$ for in-plane transport in (a) pristine and graphene-adsorbed $SrTiO_3$ and (b) La-doped $SrTiO_3$ and graphene-adsorbed La-doped $SrTiO_3$ surfaces. The shaded areas represent the calculated error due to erratic convergence of the function in eq 16 with respect to the Brillouin-zone sampling mesh (Figure S12). Plot (c) shows the calculated percentage change in the average $\boldsymbol{\kappa}_{\text{latt}}/\tau^{\text{CRTA}}$ due to the addition of graphene at the two surfaces.

that we had difficulty converging the function in eq 16 with respect to the $\mathbf{q}$-point sampling mesh (see the Supporting Information), although despite this, we still predict a reduction in the $\boldsymbol{\kappa}_{\text{latt}}$ due to the graphene adsorption. This reduction is more pronounced in the case of lanthanum doping, with a predicted average reduction of 80% over the temperature range 400−1000 K compared to a 60−70% reduction without doping. This suggests a synergy between La doping and graphene addition in suppressing the thermal transport. A possible mechanism for this is that graphene increases the "effective mass" of the bulk STO modes and therefore reduces the frequency dispersion and "depresses" the mode group velocities. This would be consistent with the stronger graphene adsorption energies calculated for the La-doped surface. The predicted reduction in thermal conductivity supports the experimental work by Lin *et al.*,[13] which demonstrated a widening of the operating temperature window for graphene/

https://doi.org/10.1021/acsami.1c10865
ACS Appl. Mater. Interfaces 2021, 13, 41303−41314

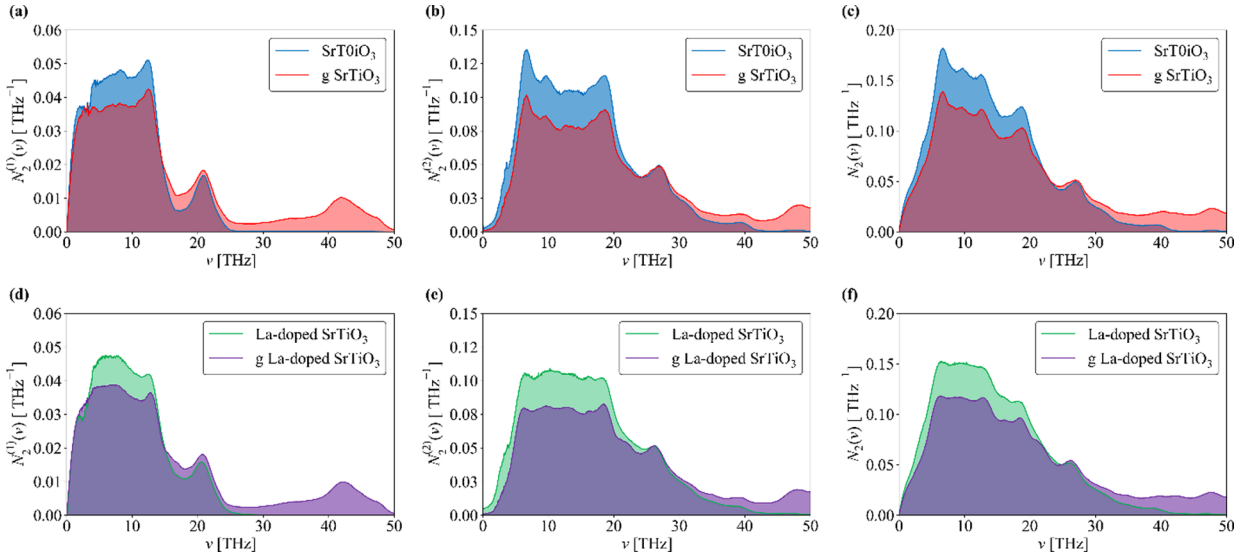

Figure 7. Weighted joint two-phonon density of states (wJDOS) for (a, d) Class 1 events ($\bar{N}_2^{(1)}$), (b, e) Class 2 events ($\bar{N}_2^{(2)}$), and (c, f) both types of event ($\bar{N}_2$) for pristine and graphene-coated $SrTiO_3$ surfaces with and without La doping.

La-doped $SrTiO_3$ samples to well below the standard operating temperature of the undoped material.

We also note in passing that the average $\boldsymbol{\kappa}_{\text{latt}}/\tau^{\text{CRTA}}$ functions suggest that La doping would lead to changes in the harmonic terms in eq 15 that would increase $\boldsymbol{\kappa}_{\text{latt}}$. However, the poor convergence behavior means this finding may not be reliable. Moreover, as suggested by the phonon DOS, it is possible that "rattling" of the La ions would counteract the increase in the harmonic terms by reducing the phonon lifetimes, leading to an overall decrease in the thermal conductivity. We explore this point further in the following.

The Γ_λ in eq 13 are computed as a sum of contributions from energy- and momentum-conserving three-phonon scattering processes between phonon triplets consisting of a reference mode λ and two interacting modes λ' and λ''. Computing the three-phonon interaction strengths $\Phi_{\lambda\lambda'\lambda''}$, which capture the strength of the physical coupling between the modes, requires the third-order force constants, and obtaining these represents a substantial computational workload. If the coupling strength can be averaged over interacting modes λ' and λ'', however, Γ_λ can be approximated as[68]

$$\tilde{\Gamma}_\lambda(\omega_\lambda) = \frac{18\pi}{\hbar} P_\lambda N_2(\mathbf{q}_\lambda, \omega_\lambda) \tag{17}$$

P_λ is the averaged phonon−phonon interaction strength defined as

$$P_\lambda = \frac{1}{(3n_a)^2} \sum_{\lambda'\lambda''} |\boldsymbol{\Phi}_{\lambda\lambda'\lambda''}|^2 \tag{18}$$

where n_a is the number of atoms in the primitive cell, and hence $3n_a$ is the number of phonon bands at each wavevector $\mathbf{q}$. $N_2(\mathbf{q}, \omega)$ is the weighted two-phonon density of states (wJDOS) and is a sum of two functions for collision (Class 1) and decay processes (Class 2)

$$N_2(\mathbf{q}, \omega) = N_2^{(1)}(\mathbf{q}, \omega) + N_2^{(2)}(\mathbf{q}, \omega) \tag{19}$$

$$N_2^{(1)}(\mathbf{q}, \omega) = \frac{1}{N} \sum_{\lambda'\lambda''} \Delta(-\mathbf{q} + \mathbf{q}' + \mathbf{q}'') \times (n_{\lambda'} - n_{\lambda''}) [\delta(\omega + \omega_{\lambda'} - \omega_{\lambda''}) - \delta(\omega - \omega_{\lambda'} + \omega_{\lambda''})] \tag{20}$$

$$N_2^{(2)}(\mathbf{q}, \omega) = \frac{1}{N} \sum_{\lambda'\lambda''} \Delta(-\mathbf{q} + \mathbf{q}' + \mathbf{q}'') \times (n_{\lambda'} + n_{\lambda''} + 1)\delta(\omega - \omega_{\lambda'} - \omega_{\lambda''}) \tag{21}$$

Here, the two functions Δ and δ enforce the conservation of (crystal) momentum and energy, respectively, and $N_2^{(1)}$ and $N_2^{(2)}$ count the number of energy- and momentum-conserving scattering processes for a reference mode with wavevector $\mathbf{q}$ and frequency ω. For making comparisons between systems, it is useful to further average the wJDOS functions over wavevectors to obtain functions of frequency only, i.e.,

$$\bar{N}_2(\omega) = \bar{N}_2^{(1)}(\omega) + \bar{N}_2^{(2)}(\omega) = \frac{1}{N} \sum_{\mathbf{q}} N_2^{(1)}(\mathbf{q}, \omega) + \frac{1}{N} \sum_{\mathbf{q}} N_2^{(2)}(\mathbf{q}, \omega) \tag{22}$$

The phonon line widths (inverse lifetimes) can thus be separated into contributions from how strongly the modes interact, and contributions from the conservation of energy, due to the shape of the phonon spectrum, which are captured by the wJDOS.[68,89] Unlike P_λ in eq 18, $\bar{N}_2(\omega)$ can be computed from the harmonic phonon frequencies. Figure 7 shows the calculated $\bar{N}_2^{(1)}$ and $\bar{N}_2^{(2)}$ for the $SrTiO_3$ surface with and without La doping and adsorbed graphene, generated using a sampling mesh with 8 × 8 × 1 wavevectors (convergence tests are shown in Figure S13). To allow for comparison between systems, we have normalized the wJDOS functions by $(3n_a)^2$, which is usually folded into the P_λ term in the expression for the approximate linewidth (cf. eq 18).

This method allows us to assess whether changes to the harmonic phonon spectrum are likely to increase/decrease the phonon linewidths and thereby decrease/increase the lifetimes. Since the thermal conductivity is proportional to the lifetimes, this can be a useful means to qualitatively compare how

https://doi.org/10.1021/acsami.1c10865
ACS Appl. Mater. Interfaces 2021, 13, 41303−41314

different dopants might affect the heat transport without the computational expense of a full third-order calculation. Peaks in $\bar{N}_2(\omega)$ at low frequencies are potentially indicative of enhanced acoustic-mode broadening; since these modes typically make the largest contributions to the thermal conductivity, this would suppress the overall heat transport.[89] However, Figure 7 shows that adsorption of graphene tends to decrease the $\bar{N}_2(\omega)$ at low frequencies. Similarly, comparing between the pure $SrTiO_3$ and La-doped systems suggests that the doping also has little effect on the wJDOS. This suggests that either the changes to the group velocities noted above are the dominant mechanism for the reduced thermal conductivity of the composites observed by Lin *et al.*[13] or that changes to the frequency spectrum/wJDOS are secondary to changes in interaction strengths in reducing the phonon lifetimes in the composites and doped samples. In particular, our calculations do not indicate significant changes in the harmonic terms between the pristine and La-doped surface models without graphene, and the wJDOS functionals also seem to be generally smaller, so we might infer from this that any reduction in the thermal conductivity on doping may be attributed to stronger phonon−phonon interactions. To investigate this further would require explicit computation of the third-order force constants, which, as noted above, is presently not practical.

CONCLUSIONS

We have performed a detailed study of how the adsorption of graphene at the surface of $SrTiO_3$ and La-doped $SrTiO_3$ affects the electronic structure, transport properties, structural dynamics, and lattice thermal conductivity. Based on our results, we draw three main conclusions from our study.

First, there is a thermodynamic driving force for graphene to adsorb to the surfaces of $SrTiO_3$ and La-doped $SrTiO_3$, yielding favorable adsorption energies.

Second, we find that the adsorption of graphene introduces C 2p states into the $SrTiO_3$ band gap, which would account for the reduced Seebeck coefficient observed by Lin *et al.*,[13] but which is likely mitigated experimentally by using smaller amounts of graphene in the composites. This highlights the sensitivity of the electrical properties to the amount and quality of the graphene in the composite and indicates that controlling this may be a simple route to fine-tuning the thermoelectric properties. Our calculations predict that extended graphene layers will induce a change from semiconducting to semimetallic behavior. However, understanding whether this behavior is localized at interfaces or extends into the bulk will require input from both experiments and modeling to elucidate the impact of different graphene concentrations on the properties of the composite.

Finally, analysis of the phonon spectra shows a remarkable reduction in the phonon group velocities on graphene adsorption, which we predict to lead to decreases of 60−90% of the bulk lattice thermal conductivity. This effect appears to be enhanced by La doping. Furthermore, analysis of the phonon spectra suggests that both La doping and graphene adsorption introduce low-frequency modes into the density of states. The former, in particular, hints at low-frequency "rattling" modes in La-doped systems that could couple to acoustic modes and suppress the phonon lifetimes. While calculations of the two-phonon density of states do not suggest enhanced acoustic-mode broadening in La-doped or graphene-adsorbed systems, it is possible that a reduction in the mode lifetimes may instead be facilitated by stronger phonon−phonon interactions. This can potentially be investigated in the future by explicit calculation of the third-order force constants.

ASSOCIATED CONTENT

Supporting Information

The Supporting Information is available free of charge at https://pubs.acs.org/doi/10.1021/acsami.1c10865.

A detailed description of electronic transport calculations performed using the BoltzWann code and comparison to results obtained with BoltzTraP; additional data from BoltzTraP transport calculations; conversion of the in-plane thermal conductivity of the rotated slab model to the bulk $SrTiO_3$ axes; and convergence of the harmonic CRTA function in eq 16 and wJDOS functions in eq 22 with respect to the **q**-point sampling mesh (PDF)

AUTHOR INFORMATION

Corresponding Authors

Jonathan M. Skelton − *Department of Chemistry, University of Manchester, Manchester M13 9PL, U.K.;* orcid.org/0000-0002-0395-1202; Email: jonathan.skelton@manchester.ac.uk

Marco Molinari − *Department of Chemical Sciences, University of Huddersfield, Queensgate, Huddersfield HD1 3DH, U.K.;* orcid.org/0000-0001-7144-6075; Email: m.molinari@hud.ac.uk

Authors

Joshua Tse − *Department of Chemical Sciences, University of Huddersfield, Queensgate, Huddersfield HD1 3DH, U.K.;* orcid.org/0000-0002-1320-557X

Alex Aziz − *Department of Chemistry, Queen Mary University of London, London E1 4NS, U.K.;* orcid.org/0000-0002-6723-9871

Joseph M. Flitcroft − *Department of Chemical Sciences, University of Huddersfield, Queensgate, Huddersfield HD1 3DH, U.K.; Department of Chemistry, University of Manchester, Manchester M13 9PL, U.K.;* orcid.org/0000-0001-8373-0233

Lisa J. Gillie − *Department of Chemical Sciences, University of Huddersfield, Queensgate, Huddersfield HD1 3DH, U.K.*

Stephen C. Parker − *Department of Chemistry, University of Bath, Bath BA2 7AY, U.K.*

David J. Cooke − *Department of Chemical Sciences, University of Huddersfield, Queensgate, Huddersfield HD1 3DH, U.K.*

Complete contact information is available at: https://pubs.acs.org/10.1021/acsami.1c10865

Author Contributions

[⊥]J.T, A.A., and J.M.F. contributed equally to this work.

Notes

The authors declare no competing financial interest.

Raw data from this study is available from the authors on reasonable request.

ACKNOWLEDGMENTS

J.M.S. is grateful to UK Research and Innovation (UKRI) for the award of a Future Leaders Fellowship (MR/T043121/1), and to the University of Manchester for the previous support of a UoM Presidential Fellowship. S.C.P. thanks the EPSRC

for funding (EP/P007821/1). Calculations were performed on the Balena HPC facility at the University of Bath, the Orion computing facility at the University of Huddersfield, the ARCHER UK National Supercomputing Service *via* our membership of the UK HEC Materials Chemistry Consortium (MCC; EPSRC EP/L000202, EP/R029431, EP/T022213), and the THOMAS facility at the UK Materials and Molecular Modelling Hub (MMM hub; EPSRC EP/P020194/1). The authors would also like to acknowledge computing time granted through the Spanish Supercomputing Network, RES, on the Tirant 3 supercomputer located at the University of Valencia (QS-2019-3-0025 and QS-2020-1-0021). Finally, this work also used the Isambard UK National Tier-2 HPC Service (http://gw4.ac.uk/isambard/) *via* the Resource Allocation Panel (RAP) Open Access to Tier-2 call, operated by the GW4 and the UK Met Office and funded by the EPSRC (EP/P020224/1).

REFERENCES

(1) Freer, R.; Powell, A. V. Realising the Potential of Thermoelectric Technology: A Roadmap. *J. Mater. Chem. C* **2020**, *8*, 441−463.
(2) Bell, L. E. Cooling, Heating, Generating Power, and Recovering Waste Heat with Thermoelectric Systems. *Science* **2008**, *321*, 1457−1461.
(3) Anatychuk, L. I.; Rozver, Y. Y.; Velichuk, D. D. Thermoelectric Generator for a Stationary Diesel Plant. *J. Electron. Mater.* **2011**, *40*, 1206−1208.
(4) Yang, J.; Stabler, F. R. Automotive Applications of Thermoelectric Materials. *J. Electron. Mater.* **2009**, *38*, 1245−1251.
(5) Kim, S. K.; Won, B. C.; Rhi, S. H.; Kim, S. H.; Yoo, J. H.; Jang, J. C. Thermoelectric Power Generation System for Future Hybrid Vehicles Using Hot Exhaust Gas. *J. Electron. Mater.* **2011**, *40*, 778−783.
(6) Azough, F.; Gholinia, A.; Alvarez-Ruiz, D. T.; Duran, E.; Kepaptsoglou, D. M.; Eggeman, A. S.; Ramasse, Q. M.; Freer, R. Self-Nanostructuring in $SrTiO_3$: A Novel Strategy for Enhancement of Thermoelectric Response in Oxides. *ACS Appl. Mater. Interfaces* **2019**, *11*, 32833−32843.
(7) Srivastava, D.; Norman, C.; Azough, F.; Schäfer, M. C.; Guilmeau, E.; Freer, R. Improving the Thermoelectric Properties of $SrTiO_3$-Based Ceramics with Metallic Inclusions. *J. Alloys Compd.* **2018**, *731*, 723−730.
(8) Srivastava, D.; Norman, C.; Azough, F.; Ekren, D.; Chen, K.; Reece, M. J.; Kinloch, I. A.; Freer, R. Anisotropy and Enhancement of Thermoelectric Performance of $Sr_{0.8}La_{0.067}Ti_{0.8}Nb_{0.2}O_{3-\delta}$ Ceramics by Graphene Additions. *J. Mater. Chem. A* **2019**, *7*, 24602−24613.
(9) Lin, Y.; Dylla, M. T.; Kuo, J. J.; Male, J. P.; Kinloch, I. A.; Freer, R.; Snyder, G. J. Graphene/Strontium Titanate: Approaching Single Crystal−Like Charge Transport in Polycrystalline Oxide Perovskite Nanocomposites through Grain Boundary Engineering. *Adv. Funct. Mater.* **2020**, *30*, No. 1910079.
(10) Yeandel, S. R.; Molinari, M.; Parker, S. C. The Impact of Tilt Grain Boundaries on the Thermal Transport in Perovskite $SrTiO_3$ Layered Nanostructures. A Computational Study. *Nanoscale* **2018**, *10*, 15010−15022.
(11) Yeandel, S. R.; Molinari, M.; Parker, S. C. Nanostructuring Perovskite Oxides: The Impact of $SrTiO_3$ Nanocube 3D Self-Assembly on Thermal Conductivity. *RSC Adv.* **2016**, *6*, 114069−114077.
(12) Koumoto, K.; Wang, Y.; Zhang, R.; Kosuga, A.; Funahashi, R. Oxide Thermoelectric Materials: A Nanostructuring Approach. *Annu. Rev. Mater. Res.* **2010**, *40*, 363−394.
(13) Lin, Y.; Norman, C.; Srivastava, D.; Azough, F.; Wang, L.; Robbins, M.; Simpson, K.; Freer, R.; Kinloch, I. A. Thermoelectric Power Generation from Lanthanum Strontium Titanium Oxide at Room Temperature through the Addition of Graphene. *ACS Appl. Mater. Interfaces* **2015**, *7*, 15898−15908.
(14) Okhay, O.; Zlotnik, S.; Xie, W.; Orlinski, K.; Hortiguela Gallo, M. J.; Otero-Irurueta, G.; Fernandes, A. J. S.; Pawlak, D. A.; Weidenkaff, A.; Tkach, A. Thermoelectric Performance of Nb-Doped $SrTiO_3$ Enhanced by Reduced Graphene Oxide and Sr Deficiency Cooperation. *Carbon* **2019**, *143*, 215−222.
(15) Shen, J. J.; Zhu, T. J.; Zhao, X. B.; Zhang, S. N.; Yang, S. H.; Yin, Z. Z. Recrystallization Induced in Situ Nanostructures in Bulk Bismuth Antimony Tellurides: A Simple Top down Route and Improved Thermoelectric Properties. *Energy Environ. Sci.* **2010**, *3*, 1519−1523.
(16) He, W.; Wang, D.; Wu, H.; Xiao, Y.; Zhang, Y.; He, D.; Feng, Y.; Hao, Y. J.; Dong, J. F.; Chetty, R.; Hao, L.; Chen, D.; Qin, J.; Yang, Q.; Li, X.; Song, J. M.; Zhu, Y.; Xu, W.; Niu, C.; Li, X.; Wang, G.; Liu, C.; Ohta, M.; Pennycook, S. J.; He, J.; Li, J. F.; Zhao, L. D. High Thermoelectric Performance in Low-Cost $SnS_{0.91}Se_{0.09}$ Crystals. *Science* **2019**, *365*, 1418−1424.
(17) Shenoy, U. S.; Bhat, D. K. Electronic Structure Modulation of $Pb_{0.6}Sn_{0.4}Te$ via Zinc Doping and Its Effect on the Thermoelectric Properties. *J. Alloys Compd.* **2021**, *872*, No. 159681.
(18) Bhat, D. K.; Shenoy, U. S. SnTe Thermoelectrics: Dual Step Approach for Enhanced Performance. *J. Alloys Compd.* **2020**, *834*, No. 155181.
(19) Tippireddy, S.; Prem Kumar, D. S.; Das, S.; Mallik, R. C. Oxychalcogenides as Thermoelectric Materials: An Overview. *ACS Applied Energy Materials*; American Chemical Society, 2021 pp 2022−2040.
(20) Caballero-Calero, O.; Ares, J. R.; Martín-González, M. Environmentally Friendly Thermoelectric Materials: High Performance from Inorganic Components with Low Toxicity and Abundance in the Earth. In *Advanced Sustainable Systems*; John Wiley & Sons, Ltd., 2021; 2100095.
(21) Fergus, J. W. Oxide Materials for High Temperature Thermoelectric Energy Conversion. *J. Eur. Ceram. Soc.* **2012**, *32*, 525−540.
(22) Prasad, R.; Bhame, S. D. Review on Texturization Effects in Thermoelectric Oxides. In *Materials for Renewable and Sustainable Energy*; Springer, 2020; pp 1−22.
(23) Srivastava, D.; Azough, F.; Freer, R.; Combe, E.; Funahashi, R.; Kepaptsoglou, D. M.; Ramasse, Q. M.; Molinari, M.; Yeandel, S. R.; Baran, J. D.; Parker, S. C. Crystal Structure and Thermoelectric Properties of Sr-Mo Substituted $CaMnO_3$: A Combined Experimental and Computational Study. *J. Mater. Chem. C* **2015**, *3*, 12245−12259.
(24) Srivastava, D.; Azough, F.; Molinari, M.; Parker, S. C.; Freer, R. High-Temperature Thermoelectric Properties of $(1 - x)$ $SrTiO_3$ − (x) $La_{1/3}NbO_3$ Ceramic Solid Solution. *J. Electron. Mater.* **2015**, *44*, 1803−1808.
(25) Wang, Y. F.; Lee, K. H.; Ohta, H.; Koumoto, K. Fabrication and Thermoelectric Properties of Heavily Rare-Earth Metal-Doped $SrO(SrTiO_3)_n$ (n = 1, 2) Ceramics. *Ceram. Int.* **2008**, *34*, 849−852.
(26) Shenoy, U. S.; Bhat, D. K. Enhanced Thermoelectric Properties of Vanadium Doped $SrTiO_3$: A Resonant Dopant Approach. *J. Alloys Compd.* **2020**, *832*, No. 154958.
(27) Shenoy, U. S.; Bhat, D. K. Electronic Structure Engineering of $SrTiO_3$ via Rhodium Doping: A DFT Study. *J. Phys. Chem. Solids* **2021**, *148*, No. 109708.
(28) Baran, J. D.; Molinari, M.; Kulwongwit, N.; Azough, F.; Freer, R.; Kepaptsoglou, D.; Ramasse, Q. M.; Parker, S. C. Tuning Thermoelectric Properties of Misfit Layered Cobaltites by Chemically Induced Strain. *J. Phys. Chem. C* **2015**, *119*, 21818−21827.
(29) Shenoy, U. S.; Bhat, D. K. Vanadium-Doped $BaTiO_3$ as High Performance Thermoelectric Material: Role of Electronic Structure Engineering. *Mater. Today Chem.* **2020**, *18*, No. 100384.
(30) Azough, F.; Cernik, R. J.; Schaffer, B.; Kepaptsoglou, D.; Ramasse, Q. M.; Bigatti, M.; Ali, A.; MacLaren, I.; Barthel, J.; Molinari, M.; Baran, J. D.; Parker, S. C.; Freer, R. Tungsten Bronze Barium Neodymium Titanate ($Ba_{6-3n}Nd_{8+2n}Ti_{18}O_{54}$): An Intrinsic Nanostructured Material and Its Defect Distribution. *Inorg. Chem.* **2016**, *55*, 3338−3350.

https://doi.org/10.1021/acsami.1c10865
ACS Appl. Mater. Interfaces 2021, 13, 41303−41314

(31) Azough, F.; Freer, R.; Yeandel, S. R.; Baran, J. D.; Molinari, M.; Parker, S. C.; Guilmeau, E.; Kepaptsoglou, D.; Ramasse, Q.; Knox, A.; Gregory, D.; Paul, D.; Paul, M.; Montecucco, A.; Siviter, J.; Mullen, P.; Li, W.; Han, G.; Man, E. A.; Baig, H.; Mallick, T.; Sellami, N.; Min, G.; Sweet, T. $Ba_{6-3x}Nd_{8+2x}Ti_{18}O_{54}$ Tungsten Bronze: A New High-Temperature *n*-Type Oxide Thermoelectric. *J. Electron. Mater.* **2016**, *45*, 1894−1899.
(32) Baran, J. D.; Kepaptsoglou, D.; Molinari, M.; Kulwongwit, N.; Azough, F.; Freer, R.; Ramasse, Q. M.; Parker, S. C. Role of Structure and Defect Chemistry in High-Performance Thermoelectric Bismuth Strontium Cobalt Oxides. *Chem. Mater.* **2016**, *28*, 7470−7478.
(33) Ahmad, A.; Hussain, M.; Zhou, Z.; Liu, R.; Lin, Y. H.; Nan, C. W. Thermoelectric Performance Enhancement of Vanadium Doped n-Type In_2O_3 Ceramics via Carrier Engineering and Phonon Suppression. *ACS Appl. Energy Mater.* **2020**, *3*, 1552−1558.
(34) Kepaptsoglou, D.; Baran, J. D.; Azough, F.; Ekren, D.; Srivastava, D.; Molinari, M.; Parker, S. C.; Ramasse, Q. M.; Freer, R. Prospects for Engineering Thermoelectric Properties in $La_{1/3}NbO_3$ Ceramics Revealed via Atomic-Level Characterization and Modeling. *Inorg. Chem.* **2018**, *57*, 45−55.
(35) Pourkiaei, S. M.; Ahmadi, M. H.; Sadeghzadeh, M.; Moosavi, S.; Pourfayaz, F.; Chen, L.; Pour Yazdi, M. A.; Kumar, R. Thermoelectric Cooler and Thermoelectric Generator Devices: A Review of Present and Potential Applications, Modeling and Materials. *Energy* **2019**, *186*, No. 115849.
(36) Wei, J.; Yang, L.; Ma, Z.; Song, P.; Zhang, M.; Ma, J.; Yang, F.; Wang, X. Review of Current High-ZT Thermoelectric Materials. *Journal of Materials Science*; Springer, 2020; pp 12642−12704.
(37) Kovalevsky, A. V.; Yaremchenko, A. A.; Populoh, S.; Thiel, P.; Fagg, D. P.; Weidenkaff, A.; Frade, J. R. Towards a High Thermoelectric Performance in Rare-Earth Substituted $SrTiO_3$: Effects Provided by Strongly-Reducing Sintering Conditions. *Phys. Chem. Chem. Phys.* **2014**, *16*, 26946−26954.
(38) Wang, H. C.; Wang, C. L.; Su, W. B.; Liu, J.; Sun, Y.; Peng, H.; Mei, L. M. Doping Effect of La and Dy on the Thermoelectric Properties of $SrTiO_3$. *J. Am. Ceram. Soc.* **2011**, *94*, 838−842.
(39) Azough, F.; Jackson, S. S.; Ekren, D.; Freer, R.; Molinari, M.; Yeandel, S. R.; Panchmatia, P. M.; Parker, S. C.; Maldonado, D. H.; Kepaptsoglou, D. M.; Ramasse, Q. M. Concurrent La and A-Site Vacancy Doping Modulates the Thermoelectric Response of $SrTiO_3$: Experimental and Computational Evidence. *ACS Appl. Mater. Interfaces* **2017**, *9*, 41988−42000.
(40) Ohta, S.; Nomura, T.; Ohta, H.; Koumoto, K. High-Temperature Carrier Transport and Thermoelectric Properties of Heavily La- Or Nb-Doped $SrTiO_3$ Single Crystals. *J. Appl. Phys.* **2005**, *97*, No. 34106.
(41) Ohta, S.; Nomura, T.; Ohta, H.; Hirano, M.; Hosono, H.; Koumoto, K. Large Thermoelectric Performance of Heavily Nb-Doped $SrTiO_3$ Epitaxial Film at High Temperature. *Appl. Phys. Lett.* **2005**, *87*, No. 092108.
(42) Ohta, S.; Ohta, H.; Koumoto, K. Grain Size Dependence of Thermoelectric Performance of Nb-Doped $SrTiO_3$ Polycrystals. *J. Ceram. Soc. Japan* **2006**, *114*, 102−105.
(43) Wan, C.; Wang, Y.; Wang, N.; Norimatsu, W.; Kusunoki, M.; Koumoto, K. Development of Novel Thermoelectric Materials by Reduction of Lattice Thermal Conductivity. *Sci. Technol. Adv. Mater.* **2010**, *11*, No. 044306.
(44) Zhang, L.; Lü, T. Y.; Wang, H. Q.; Zhang, W. X.; Yang, S. W.; Zheng, J. C. First Principles Studies on the Thermoelectric Properties of $(SrO)_m(SrTiO_3)_n$ Superlattice. *RSC Adv.* **2016**, *6*, 102172−102182.
(45) Zou, D.; Liu, Y.; Xie, S.; Lin, J.; Li, J. Effect of Strain on Thermoelectric Properties of $SrTiO_3$: First-Principles Calculations. *Chem. Phys. Lett.* **2013**, *586*, 159−163.
(46) Dylla, M. T.; Kuo, J. J.; Witting, I.; Snyder, G. J. Grain Boundary Engineering Nanostructured $SrTiO_3$ for Thermoelectric Applications. In*Advanced Materials Interfaces*; John Wiley & Sons, Ltd., 2019; 1900222.
(47) Huang, J.; Yan, P.; Liu, Y.; Xing, J.; Gu, H.; Fan, Y.; Jiang, W. Simultaneously Breaking the Double Schottky Barrier and Phonon Transport in $SrTiO_3$-Based Thermoelectric Ceramics via Two-Step Reduction. *ACS Appl. Mater. Interfaces* **2020**, *12*, 52721−52730.
(48) Dong, J.; Liu, W.; Li, H.; Su, X.; Tang, X.; Uher, C. In Situ Synthesis and Thermoelectric Properties of PbTe-Graphene Nanocomposites by Utilizing a Facile and Novel Wet Chemical Method. *J. Mater. Chem. A* **2013**, *1*, 12503−12511.
(49) Ahmad, K.; Wan, C.; Al-Eshaikh, M. A.; Kadachi, A. N. Enhanced Thermoelectric Performance of Bi_2Te_3 Based Graphene Nanocomposites. *Appl. Surf. Sci.* **2019**, *474*, 2−8.
(50) Bantawal, H.; Sethi, M.; Shenoy, U. S.; Bhat, D. K. Porous Graphene Wrapped $SrTiO_3$ Nanocomposite: Sr-C Bond as an Effective Coadjutant for High Performance Photocatalytic Degradation of Methylene Blue. *ACS Appl. Nano Mater.* **2019**, *2*, 6629−6636.
(51) Feng, X.; Fan, Y.; Nomura, N.; Kikuchi, K.; Wang, L.; Jiang, W.; Kawasaki, A. Graphene Promoted Oxygen Vacancies in Perovskite for Enhanced Thermoelectric Properties. *Carbon* **2017**, *112*, 169−176.
(52) Baran, J. D.; Eames, C.; Takahashi, K.; Molinari, M.; Islam, M. S.; Parker, S. C. Structural, Electronic, and Transport Properties of Hybrid $SrTiO_3$-Graphene and Carbon Nanoribbon Interfaces. *Chem. Mater.* **2017**, *29*, 7364−7370.
(53) Kresse, G.; Furthmüller, J. Efficiency of Ab-Initio Total Energy Calculations for Metals and Semiconductors Using a Plane-Wave Basis Set. *Comput. Mater. Sci.* **1996**, *6*, 15−50.
(54) Kresse, G.; Hafner, J. *Ab Initio* Molecular Dynamics for Liquid Metals. *Phys. Rev. B* **1993**, *47*, 558−561.
(55) Kresse, G.; Hafner, J. *Ab Initio* Molecular-Dynamics Simulation of the Liquid-Metal-Amorphous- Semiconductor Transition in Germanium. *Phys. Rev. B* **1994**, *49*, 14251−14269.
(56) Kresse, G.; Furthmüller, J. Efficient Iterative Schemes for *Ab Initio* Total-Energy Calculations Using a Plane-Wave Basis Set. *Phys. Rev. B* **1996**, *54*, 11169−11186.
(57) Perdew, J. P.; Burke, K.; Ernzerhof, M. Generalized Gradient Approximation Made Simple. *Phys. Rev. Lett.* **1996**, *77*, 3865−3868.
(58) Perdew, J. P.; Burke, K.; Ernzerhof, M. Erratum: Generalized Gradient Approximation Made Simple. *Phys. Rev. Lett.* **1996**, *77*, 3865.
(59) Grimme, S.; Antony, J.; Ehrlich, S.; Krieg, H. A Consistent and Accurate *Ab Initio* Parametrization of Density Functional Dispersion Correction (DFT-D) for the 94 Elements H-Pu. *J. Chem. Phys.* **2010**, *132*, No. 154104.
(60) Kresse, G.; Joubert, D. From Ultrasoft Pseudopotentials to the Projector Augmented-Wave Method. *Phys. Rev. B* **1999**, *59*, 1758−1775.
(61) Blöchl, P. E. Projector Augmented-Wave Method. *Phys. Rev. B* **1994**, *50*, 17953−17979.
(62) Madsen, G. K. H.; Singh, D. J. BoltzTraP. A Code for Calculating Band-Structure Dependent Quantities. *Comput. Phys. Commun.* **2006**, *175*, 67−71.
(63) Pizzi, G.; Volja, D.; Kozinsky, B.; Fornari, M.; Marzari, N. BoltzWann: A Code for the Evaluation of Thermoelectric and Electronic Transport Properties with a Maximally-Localized Wannier Functions Basis. *Comput. Phys. Commun.* **2014**, *185*, 422−429.
(64) Pizzi, G.; Volja, D.; Kozinsky, B.; Fornari, M.; Marzari, N. An Updated Version of BOLTZWANN: A Code for the Evaluation of Thermoelectric and Electronic Transport Properties with a Maximally-Localized Wannier Functions Basis. *Comput. Phys. Commun.* **2014**, *185*, 2311−2312.
(65) Molinari, M.; Tompsett, D. A.; Parker, S. C.; Azough, F.; Freer, R. Structural, Electronic and Thermoelectric Behaviour of $CaMnO_3$ and $CaMnO_{(3-\delta)}$. *J. Mater. Chem. A* **2014**, *2*, 14109−14117.
(66) Togo, A.; Tanaka, I. First Principles Phonon Calculations in Materials Science. *Scr. Mater.* **2015**, *108*, 1−5.
(67) Parlinski, K.; Li, Z. Q.; Kawazoe, Y. First-Principles Determination of the Soft Mode in Cubic ZrO_2. *Phys. Rev. Lett.* **1997**, *78*, 4063−4066.
(68) Togo, A.; Chaput, L.; Tanaka, I. Distributions of Phonon Lifetimes in Brillouin Zones. *Phys. Rev. B* **2015**, *91*, 94306.
(69) Staykov, A.; Tellez, H.; Druce, J.; Wu, J.; Ishihara, T.; Kilner, J. Electronic Properties and Surface Reactivity of SrO-Terminated

https://doi.org/10.1021/acsami.1c10865
ACS Appl. Mater. Interfaces 2021, 13, 41303−41314

$SrTiO_3$ and SrO-Terminated Iron-Doped $SrTiO_3$. *Sci. Technol. Adv. Mater.* **2018**, *19*, 221−230.
(70) Druce, J.; Téllez, H.; Burriel, M.; Sharp, M. D.; Fawcett, L. J.; Cook, S. N.; McPhail, D. S.; Ishihara, T.; Brongersma, H. H.; Kilner, J. A. Surface Termination and Subsurface Restructuring of Perovskite-Based Solid Oxide Electrode Materials. *Energy Environ. Sci.* **2014**, *7*, 3593−3599.
(71) Chen, Y.; Téllez, H.; Burriel, M.; Yang, F.; Tsvetkov, N.; Cai, Z.; McComb, D. W.; Kilner, J. A.; Yildiz, B. Segregated Chemistry and Structure on (001) and (100) Surfaces of $(La_{1-x}Sr_x)_2CoO_4$ Override the Crystal Anisotropy in Oxygen Exchange Kinetics. *Chem. Mater.* **2015**, *27*, 5436−5450.
(72) Burriel, M.; Wilkins, S.; Hill, J. P.; Muñoz-Márquez, M. A.; Brongersma, H. H.; Kilner, J. A.; Ryan, M. P.; Skinner, S. J. Absence of Ni on the Outer Surface of Sr Doped La_2NiO_4 Single Crystals. *Energy Environ. Sci.* **2014**, *7*, 311−316.
(73) Watson, G. W.; Kelsey, E. T.; De Leeuw, N. H.; Harris, D. J.; Parker, S. C. Atomistic Simulation of Dislocations, Surfaces and Interfaces in MgO. *J. Chem. Soc., Faraday Trans.* **1996**, *92*, 433−438.
(74) Zou, B.; Walker, C.; Wang, K.; Tileli, V.; Shaforost, O.; Harrison, N. M.; Klein, N.; Alford, N. M.; Petrov, P. K. Growth of Epitaxial Oxide Thin Films on Graphene. *Sci. Rep.* **2016**, *6*, No. 31511.
(75) Bantawal, H.; Shenoy, U. S.; Bhat, D. K. Tuning the Photocatalytic Activity of $SrTiO_3$ by Varying the Sr/Ti Ratio: Unusual Effect of Viscosity of the Synthesis Medium. *J. Phys. Chem. C* **2018**, *122*, 20027−20033.
(76) Jiao, S.; Yan, J.; Sun, G.; Zhao, Y. Electronic Structures and Optical Properties of Nb-Doped $SrTiO_3$ from First Principles. *J. Semicond.* **2016**, *37*, No. 072001.
(77) Shenoy, U. S.; Bantawal, H.; Bhat, D. K. Band Engineering of $SrTiO_3$: Effect of Synthetic Technique and Site Occupancy of Doped Rhodium. *J. Phys. Chem. C* **2018**, *122*, 27567−27574.
(78) Meyer, B.; Padilla, J.; Vanderbilt, D. Theory of $PbTiO_3$, $BaTiO_3$, and $SrTiO_3$ Surfaces. *Faraday Discuss.* **1999**, *114*, 395−405.
(79) Van Benthem, K.; Elsässer, C.; French, R. H. Bulk Electronic Structure of $SrTiO_3$: Experiment and Theory. *J. Appl. Phys.* **2001**, *90*, 6156−6164.
(80) Holmström, E.; Spijker, P.; Foster, A. S. The Interface of $SrTiO_3$ and H_2O from Density Functional Theory Molecular Dynamics. *Proc. R. Soc. A* **2016**, *472*, No. 20160293.
(81) Holmström, E.; Foster, A. S. Adsorption of Water onto $SrTiO_3$ from Periodic Møller-Plesset Second-Order Perturbation Theory. *J. Chem. Theory Comput.* **2017**, *13*, 6301−6307.
(82) Scheidemantel, T. J.; Ambrosch-Draxl, C.; Thonhauser, T.; Badding, V.; Sofo, O. Transport Coefficients from First-Principles Calculations. *Phys. Rev. B* **2003**, *68*, No. 125210.
(83) Okuda, T.; Nakanishi, K.; Miyasaka, S.; Tokura, Y. Large Thermoelectric Response of Metallic Perovskites: $Sr_{1-x}La_xTiO_3$ ($0 \leq x \leq 0.1$). *Phys. Rev. B* **2001**, *63*, No. 113104.
(84) Ravichandran, J.; Siemons, W.; Oh, D. W.; Kardel, J. T.; Chari, A.; Heijmerikx, H.; Scullin, M. L.; Majumdar, A.; Ramesh, R.; Cahill, D. G. High-Temperature Thermoelectric Response of Double-Doped $SrTiO_3$ Epitaxial Films. *Phys. Rev. B* **2010**, *82*, No. 165126.
(85) Zhang, R.-Z.; Wang, C.-L.; Li, J.-C.; Su, W.-B.; Zhang, J.-L.; Zhao, M.-L.; Liu, J.; Zhang, Y.-F.; Mei, L.-M. Determining Seebeck Coefficient of Heavily Doped La:$SrTiO_3$ from Density Functional Calculations. *Solid State Sci.* **2010**, *12*, 1168−1172.
(86) Ouyang, Y.; Guo, J. A Theoretical Study on Thermoelectric Properties of Graphene Nanoribbons. *Appl. Phys. Lett.* **2009**, *94*, No. 263107.
(87) Wood, C. Materials for Thermoelectric Energy Conversion. *Rep. Prog. Phys.* **1988**, *51*, 459−539.
(88) Tang, J.; Skelton, J. M. Impact of Noble-Gas Filler Atoms on the Lattice Thermal Conductivity of $CoSb_3$ Skutterudites: First-Principles Modelling. *J. Phys.: Condens. Matter* **2021**, *33*, No. 164002.
(89) Gold-Parker, A.; Gehring, P. M.; Skelton, J. M.; Smith, I. C.; Parshall, D.; Frost, J. M.; Karunadasa, H. I.; Walsh, A.; Toney, M. F. Acoustic Phonon Lifetimes Limit Thermal Transport in Methyl-ammonium Lead Iodide. *Proc. Natl. Acad. Sci. U.S.A.* **2018**, *115*, 11905−11910.

https://doi.org/10.1021/acsami.1c10865
ACS Appl. Mater. Interfaces 2021, 13, 41303−41314